

Enhanced bending failure strain in biological glass fibers due to internal lamellar architecture

Michael A. Monn, Haneesh Kesari*

Brown University, School of Engineering, Providence, RI, USA



ARTICLE INFO

Keywords:

Structure-property relationship
Structural biological material
Euplectella aspergillum
Tethya aurantia
Flexural strength
Spicules

ABSTRACT

The remarkable mechanical properties of biological structures, like tooth and bone, are often a consequence of their architecture. The tree ring-like layers that comprise the skeletal elements of the marine sponge *Euplectella aspergillum* are a quintessential example of the intricate architectures prevalent in biological structures. These skeletal elements, known as spicules, are hair-like fibers that consist of a concentric array of silica cylinders separated by thin, organic layers. Thousands of spicules act like roots to anchor the sponge to the sea floor. While spicules have been the subject of several structure-property investigations, those studies have mostly focused on the relationship between the spicule's layered architecture and toughness properties. In contrast, we hypothesize that the spicule's layered architecture enhances its bending failure strain, thereby allowing it to provide a better anchorage to the sea floor. We test our hypothesis by performing three-point bending tests on *E. aspergillum* spicules, measuring their bending failure strains, and comparing them to those of spicules from a related sponge, *Tethya aurantia*. The *T. aurantia* spicules have a similar chemical composition to *E. aspergillum* spicules but have no architecture. Thus, any difference between the bending failure strains of the two types of spicules can be attributed to the *E. aspergillum* spicules' layered architecture. We found that the bending failure strains of the *E. aspergillum* spicules were roughly 2.4 times larger than those of the *T. aurantia* spicules.

1. Introduction

Structural biological materials (SBMs), such as bone and shell, perform a variety of mechanical functions that include facilitating locomotion, and offering protection from predators and severe environmental conditions (Chen et al., 2008). An organism's survival depends on the mechanical performance of SBMs. Despite being composed of weak, brittle constituents (e.g., calcium carbonate and silica) SBMs possess remarkable mechanical properties, such as strength and toughness (Meyers et al., 2013; Jackson et al., 1988; Barber et al., 2015). These properties are believed to be consequences of the stunning mechanical designs prevalent in SBMs (Chen et al., 2008; Meyers et al., 2013). Specifically, SBMs are often heterogeneous and are composed of a ceramic and an organic phase that are mixed together in intricate, 3D patterns. We refer to the way that these two phases are interlaced as a SBM's architecture. Some examples of architectures in SBMs are the brick-and-mortar arrangement of ceramic tablets in nacre (Rabiei et al., 2010), and the interlocking helices of chitin in the club-like appendages of stomatopods (Weaver et al., 2012) and in beetle exocuticle (Yang et al.).

While SBMs do not outperform engineering materials, like advanced

ceramics, combining SBM architectures with modern chemistry could lead to a new generation of structural materials whose mechanical properties far exceed those of today's state-of-the-art (Espinosa et al., 2009; Wegst et al., 2015). Furthermore, by tuning the architectural parameters of a bio-inspired material (e.g., tablet aspect ratio and overlap in brick-and-mortar composites (Barthelat, 2014)), the resulting enhancement of mechanical properties can exceed that which is achieved by simply copying the SBM's architecture (Rim et al., 2011). The first step toward understanding how an architecture affects mechanical properties is quantifying the effect that the architecture has on the mechanical properties that are relevant to the SBM's primary mechanical function(s).

The skeleton of the marine sponge *Euplectella aspergillum* (*E.a.*) has served as a valuable system for studying structure-property relationships (Aizenberg et al., 2005; Weaver et al., 2007; Monn et al., 2015). *Euplectella aspergillum*'s skeleton consists of a cylindrical, cage-like assembly of filaments called spicules (see Fig. 1 (A)) (Aizenberg et al., 2005; Weaver et al., 2007). The spicules are approximately 50 μm in diameter, up to 10 cm in length, and are composed primarily of silica. While the spicules in the skeletal cage are “glued” together to form a stiff lattice, there is a tuft of free-standing spicules at the base of the

* Corresponding author.

E-mail addresses: michael_monn@brown.edu (M.A. Monn), haneesh_kesari@brown.edu (H. Kesari).

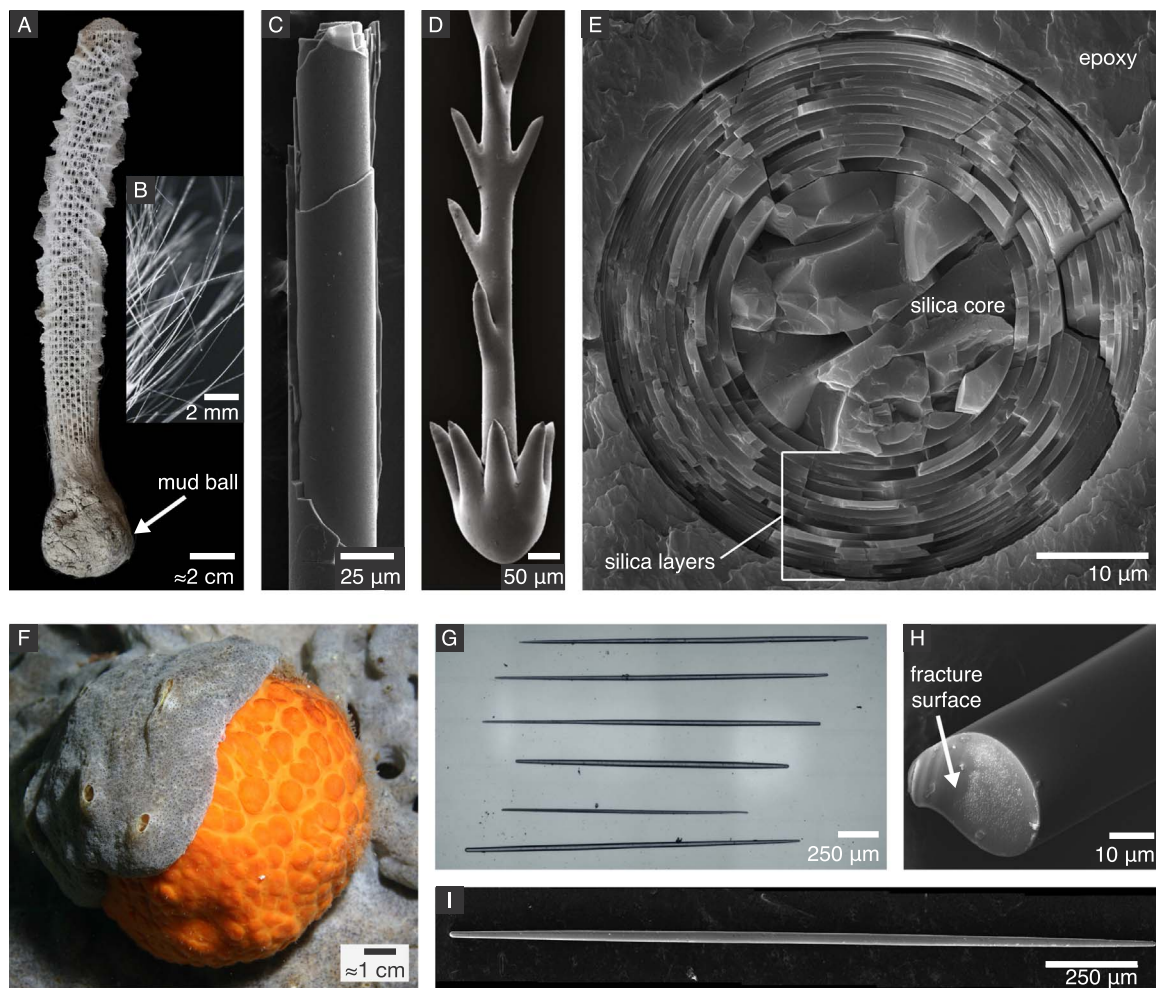


Fig. 1. Skeleton and spicules of *E. a.* and *T. a.* sponges. (A) An *E. a.* skeleton. The mud ball at the bottom of the skeleton contains the anchor spicules (courtesy of Swee Cheng Lim). (B) The anchor spicules from an *E. a.* skeleton separated from the mud ball. (C) A broken *E. a.* anchor spicule exposing its architecture. (D) The distal end of a *E. a.* anchor spicule is covered in barbs that help the spicule anchor to the sea floor. Reproduced from Aizenberg et al. (2004), Copyright 2004 National Academy of Sciences. (E) A cross-sectioned anchor spicule. Modified from Monn et al. (2015). (F) A live *T. a.* sponge (courtesy of Steve Lonhart/NOAA MBNMS). (G) Spicules from a *T. a.* sponge. (H) A fractured *T. a.* spicule. (I) The *T. a.* spicules are tapered along their length. Reproduced from Monn and Kesari under the Creative Commons 4.0 BY license.

skeleton that are used like roots to anchor the sponge to the sea floor (see Fig. 1 (A), (B)) (Weaver et al., 2007). The anchor spicules possess a concentric architecture. In cross-section, an anchor spicule consists of a $\approx 10 \mu\text{m}$ silica core that is surrounded by a coaxial assembly of ≈ 25 hollow, silica cylinders (see Fig. 1 (C), (E)). Adjacent silica cylinders are separated by a thin ($\approx 10 \text{ nm}$), protein interlayer (Weaver et al., 2007).

We investigate the hypothesis that the *E. a.* spicule's architecture enhances its bending failure strain, which allows it to provide a stronger attachment to the sea floor. Our hypothesis is motivated by several observations and deductions: (i) *The sponge obtains nutrients by filtering microorganisms from sea water. While the sponge pumps water through its body, the flow of water is facilitated by ocean currents.* We reason that in order to pump and filter water, the sponge must be robustly attached to the sea floor. (ii) *The distal ends of the E. a. anchor spicules are covered in barbs (see Fig. 1 (D)).* We believe that the orientation of these barbs implies that the spicule's primary mechanical function is to anchor the sponge to the sea floor. (iii) *Sponges have the ability to make spicules in a large variety of shapes (Weaver et al., 2010; Van Soest et al.).* The presence of the barbs, therefore, suggests that there is evolutionary pressure on the spicules to enhance their anchoring ability. (iv) *It has been shown that the force required to pull a fiber out of an elastic matrix increases with the curvature of the fiber inside the matrix (Wang et al., 2016; Chen et al., 2009).* Therefore, we deduce that spicules will be better anchors if they are able to withstand larger bending strains.

We test our hypothesis by performing three-point bending tests on *E. a.* spicules and measuring the bending strains at which they fail. In order to quantify the effect of the architecture on the strain at which *E. a.* spicules fail, we must compare them to a material that has the same intrinsic mechanical properties but which lacks architecture. We use spicules from a related sponge, *Tethya aurantia* (*T. a.*), as this control material (Sarà and Manara, 1991). *Tethya aurantia* is a spherical sponge that lives on rocky substrates in shallow, coastal water (see Fig. 1 (F)). Its skeleton consists of 2 mm long, 40 μm diameter rod-like spicules that are tapered along their length (see Fig. 1 (G), (I)) (Monn and Kesari). The *T. a.* spicules have the same bulk chemical composition and volume-averaged bonding structure as the *E. a.* spicules (Weaver et al., 2010), and are produced using a similar growth process (Leys, 2003; Müller et al., 2009). We, therefore, assume that the intrinsic mechanical properties of the *T. a.* spicules are the same as those of the *E. a.* spicules. The *T. a.* spicules, however, do not have any architecture (see Fig. 1 (H)).

We performed three-point bending tests on 33 *E. a.* and 24 *T. a.* spicules using a custom-built mechanical testing device (see Fig. 2 (A), (B)). The detailed descriptions of our mechanical testing device and test procedure are given in Section 2.2. Briefly, sections of *E. a.* spicules and *T. a.* spicules were suspended across a trench. A motorized translation stage was used to push each spicule against an aluminum wedge that was positioned midway across the trench—at mid span (see Fig. 2 (B), (D)). The force applied to the spicule by the wedge and the lateral deflection

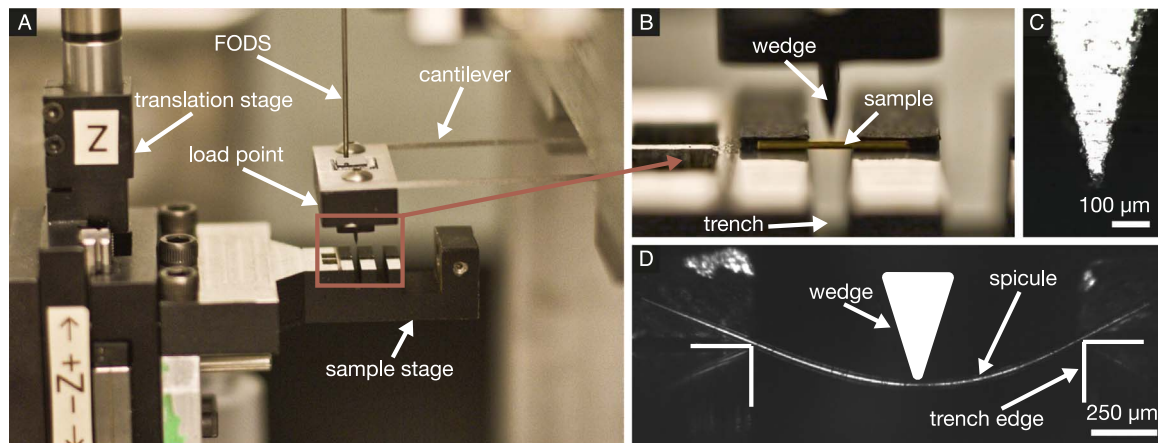


Fig. 2. Mechanical testing device. (A) The major components of the mechanical testing device are the sample stage and the load point-cantilever assembly. (B) A closer view of the wedge-like tip of the load point and the trench in the sample stage. To aid in visualization of the experimental setup, a $\approx 125 \mu\text{m}$ diameter brass wire (sample) is shown in place of a spicule. (C) A micrograph of the load point tip. (D) A micrograph of a *T.a.* spicule just before failure. The trench edges and wedge are marked schematically.

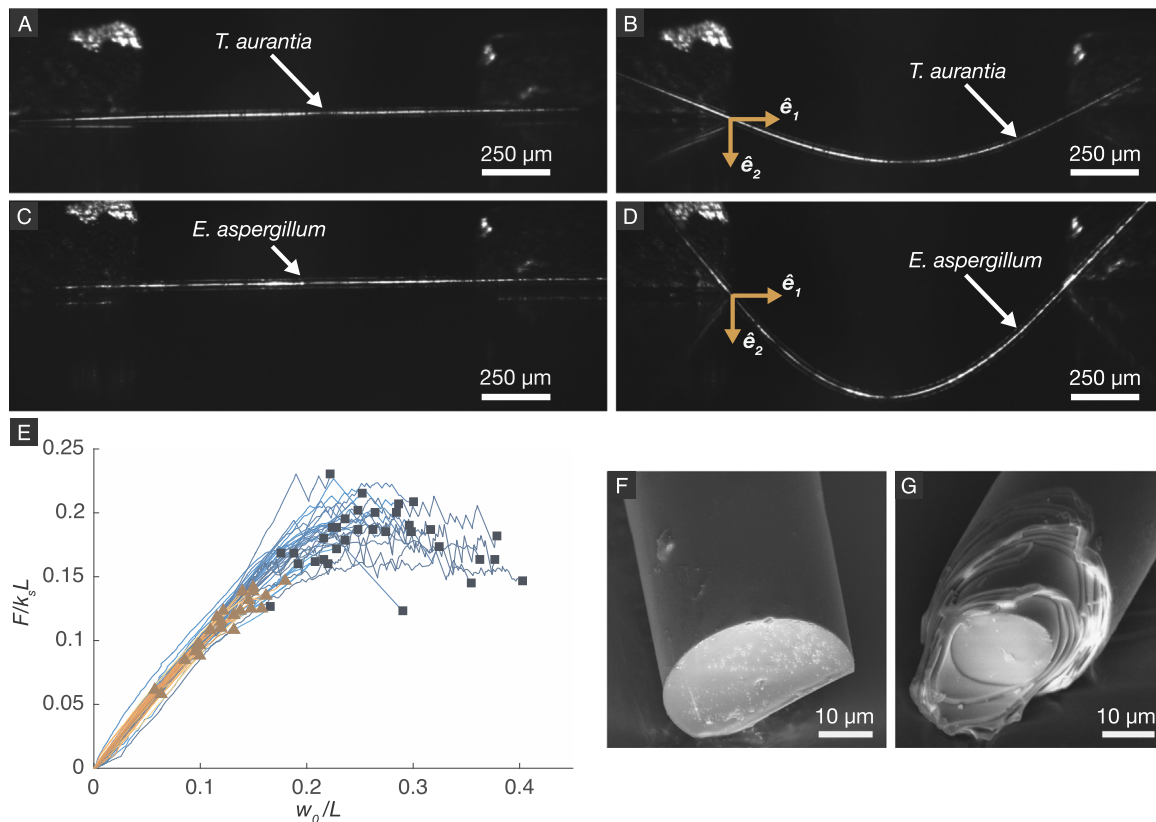


Fig. 3. Three-point bending test data. (A) and (B) (resp. (C) and (D)) show the undeformed configuration and deformed configuration just before failure of a representative *T.a.* (resp. *E.a.*) spicule. The coordinate system used to describe the position of points along a spicule's longitudinal mid-plane is shown in (B) and (D). (E) Dimensionless load-deflection data of the 33 *E.a.* (blue) and 24 *T.a.* (orange) spicules. The force and deflection at which each *T.a.* (resp. *E.a.*) spicule failed is indicated by an orange triangle (resp. dark blue square). (F) (resp. (G)) A representative fractured *T.a.* (resp. *E.a.*) spicule. (For interpretation of the references to color in this figure legend, the reader is referred to the web version of this article.)

of the spicule's cross-section that is in contact with the wedge were measured (see Section 2.2 and Fig. 3 (E)). We also imaged the spicules during the test using a reflected light microscope and used these images to compute the strain at which each spicule failed (see Fig. 3 (B), (D)).

We define a spicule's effective bending strain to be the strain in the outermost material fiber of a homogeneous beam with the same curvature and cross-sectional shape as the spicule (see Section 3). The spicule's "bending failure strain" is the maximum effective bending strain along the spicule's length before it fails. We use the following procedure to compute each spicule's bending failure strain. We select points along each spicule's longitudinal mid-plane in the micrograph

taken just before it failed (see Fig. 4 (C), (D)). We fit a polynomial function to these points and computed the curvature of the longitudinal mid-plane using this function (see Section 3 and Fig. 4 (D), (E)). After each test, we measured the radius of the cross-section at which the spicule failed from a scanning electron micrograph (see Section 2.4 and Fig. 5 (A)). Finally, we computed each spicule's bending failure strain from the maximum curvature of the polynomial function and the spicule's cross-sectional radius at the location of failure using elastica theory (see Section 3 and Fig. 5 (C)) (Dym and Shames, 1973).

By comparing the *E.a.* spicules to the *T.a.* spicules, we find that the *E.a.* spicule's concentrically layered architecture increases its bending

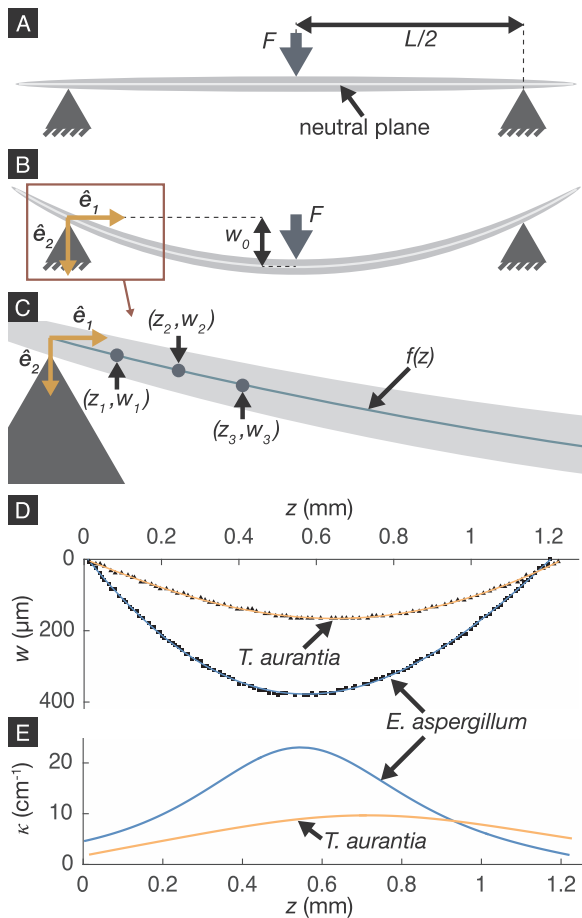


Fig. 4. Measurement of spicule curvatures from three-point bending test images. (A) Schematic of the spicule's undeformed configuration. (B) Schematic of the spicule's deformed configuration. (C) A magnified view of (B) showing the discrete representation of the spicule's longitudinal mid-plane, $(z_i, w_i)_{i=1 \dots n}$, and the continuous representation of the longitudinal mid-plane, $f(z)$. (D) The black triangles (resp. squares) correspond to the $(z_i, w_i)_{i=1 \dots n}$ for the representative *T.a.* (resp. *E.a.*) spicule shown in Fig. 3 (B) (resp. (D)). The orange (resp. blue) curves correspond to $f(z)$ for the representative *T.a.* (resp. *E.a.*) spicule. (E) the curvature, $\kappa(z)$, computed from the $f(z)$ shown in (C). (For interpretation of the references to color in this figure legend, the reader is referred to the web version of this article.)

failure strain by roughly 140%. This supports our hypothesis that the *E.a.* spicules' architecture allows them to bend more before failing, thereby allowing them to provide a better anchorage to the sea floor.

2. Materials and methods

2.1. Preparation of spicules for mechanical testing

Euplectella aspergillum spicules were removed from dried skeletons and stored at room temperature. Since the *E.a.* spicules are ≈ 10 cm long, we performed the bending tests on small (≈ 5 mm) sections of them that we cut from roughly the mid point along each spicule's length. We cut the sections using a razor blade immediately before performing the bending tests. *T. aurantia* spicules were received dried and separated from the sponge tissue, and were stored at room temperature.

Each *E.a.* spicule section and *T.a.* spicule was inspected using a polarized light microscope. Sections of *E.a.* spicules containing barbs (e.g. see Fig. 1 (D)) were discarded. Due to the fragility of the outer silica cylinders of the *E.a.* spicules, surface cracks were commonly observed. Since pristine spicules were virtually nonexistent, only sections with missing pieces of layers were discarded. *Tethya aurantia* spicules that were not completely intact were also discarded.

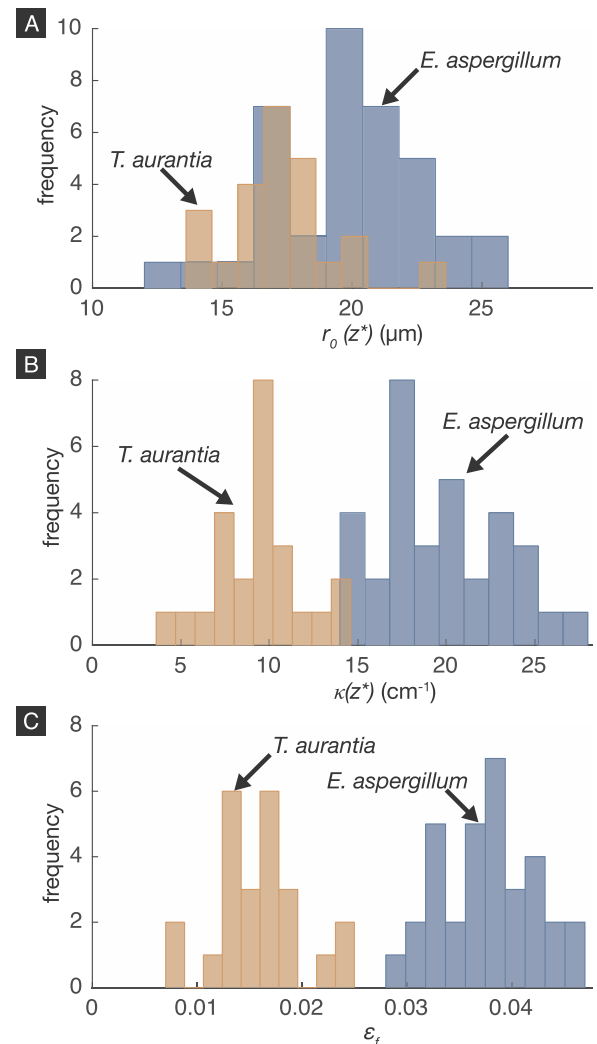


Fig. 5. Bending failure strains of *E.a.* and *T.a.* spicules. (A) A histogram of $r_0(z^*)$ for the *E.a.* and *T.a.* spicules. (B) A histogram of $\kappa(z^*)$ for the *E.a.* and *T.a.* spicules. (C) A histogram of the bending failure strains, ϵ_f , for the *E.a.* and *T.a.* spicules.

A spicule that passed this inspection procedure was placed across a trench cut in a stainless steel plate (see Fig. 2 (B)). The trench has parallel, vertical walls and the trench edges support the spicules during the three-point bending tests. The trench's span, L , was measured from optical micrographs to be $1278 \pm 3 \mu\text{m}$ (mean \pm standard deviation; $N = 10$). We ensured that each spicule's longitudinal mid-plane was perpendicular to the trench edges. Since the *T.a.* spicules are tapered, we took efforts to also ensure that the midpoint along each *T.a.* spicule's length was coincident with the trench's mid span.

2.2. Construction and operation of the mechanical testing device

Our mechanical testing device consists of two major components: a sample stage that holds the spicules (see Fig. 2 (A)), and a wedge-shaped load point (LP) that applies force to the spicules (see Fig. 2 (A)–(C)).

The sample stage consists of the steel plate containing the trench, which is attached to a three-axis translation stage that is controlled by DC servo motors. The motors have a minimum repeatable step size of 200 nm. The ends of the spicules are not affixed to the trench edges and are therefore free to rotate or slide on the trench edges. The LP's tip is an aluminum wedge that has an included angle of approximately 35 degrees. The radius of curvature of the apex of this wedge is approximately 20 μm (see Fig. 2 (C)). To perform a bending test, the LP is first

centered at the trench's mid span by finding and averaging the positions of the two trench edges. After centering, the spicule is pushed into the LP in 2 μm stage displacement increments at an average rate of 1 $\mu\text{m/s}$ until the spicule fails.

The LP is attached to the end of an aluminum cantilever, which is used as a force sensor. The operating principle of the LP-cantilever assembly is similar to that of an atomic force microscope (Cappella and Dietler, 1999). As a spicule is pushed into the LP we measure the displacement of the LP, $-w_{LP}\hat{e}_2$, using a fiber optic displacement sensor (FODS), where \hat{e}_2 is the Cartesian basis vector shown in Fig. 3 (B), (D). After each stage displacement increment, we take 100 w_{LP} measurements and average them to reduce noise caused by mechanical vibrations. Let $-w_s\hat{e}_2$ and $w_0\hat{e}_2$ be the displacements of the stage and the spicule's cross-section under the LP, respectively. Since the LP and the spicule remain in contact until failure, w_0 is given by the difference between the stage and LP displacements, or

$$w_0 = w_s - w_{LP}. \quad (1)$$

We then use the cantilever's stiffness, k_c , to compute the force applied by the LP, $F\hat{e}_2$. The cantilever deflections observed during the bending tests are small enough (roughly 1% of the cantilever's length) that the relationship between F and w_{LP} is linear. Therefore, the force is given by

$$F = k_c w_{LP}. \quad (2)$$

We hung calibration weights, whose masses we measured with ± 0.1 mg accuracy, from the end of the cantilever and measured w_{LP} . We fitted Eq. (2) to this load–displacement data to estimate k_c to be 90.6 ± 0.3 N/m. The FODS has a measurement uncertainty of roughly 220 nm and, consequently, our mechanical testing device has a force resolution of roughly 20 μN .

The load-displacement data for the *E.a.* and *T.a.* spicules are shown in Fig. 3 (E). Finally, after each displacement increment we acquire an image of the spicule's bent shape (see Fig. 3 (B), (D)) using a $5\times$ magnification reflected light microscope (Infinitube, AVT Manta). The image acquisition, FODS data acquisition and stage motion are all controlled using National Instruments LabView.

2.3. Calibration of the mechanical testing device

We calibrated the mechanical testing device by measuring the Young's modulus, E , of a tungsten wire. For the configuration shown in Fig. 4 (B), the Young's modulus is given by

$$E = k_s L^3 / 48I, \quad (3)$$

where k_s is the slope of the linear portion of the F – w_0 data, $I = \pi r_0^4 / 4$ is the second moment of area of the cross-section, L is the trench span, and r_0 is the cross-sectional radius of the wire. Eq. (3) comes from the Euler-Bernoulli theory for a simply-supported beam with a concentrated lateral load acting at mid span (Gere and Timoshenko, 1997).

We measured the wire's diameter to be 15.15 ± 0.03 μm (mean \pm standard deviation; $N = 10$) using a scanning electron microscope (SEM). We performed 12 tests on different pieces of the tungsten wire and found the Young's modulus to be 395.2 ± 13.4 GPa (mean \pm standard deviation). This value agrees closely with values cited in literature (see Table 1).

2.4. Measurement of spicule diameters

After each bending test, we collected the fragments of the broken spicule. The spicule fragments were handled exclusively using fine point brushes to avoid introducing damage to their fracture surfaces. The fragments were mounted to an aluminum stub using conductive carbon tape, sputter coated with 10 nm of carbon and imaged in a SEM. We measured the diameter of each spicule's cross-section at the location of failure from the SEM images.

Table 1

Young's modulus of tungsten (GPa).

Measured ($N = 12$)		Reference		
mean	s.d.	Bernstein (1962)	Simmons and Wang	Oliver and Pharr (1992)
395.2	13.4	404.0	409.8	410

3. Results

Fig. 4 (A) and (B) are schematics of the undeformed and deformed configurations of a spicule, respectively, in the context of our bending experiment. The edges of the trench are shown as simple supports. In the deformed configuration, the set $\{\hat{e}_1, \hat{e}_2\}$ is an orthonormal set of Cartesian basis vectors with $\{z, w\}$ being its corresponding set of Cartesian coordinates. The origin of the coordinate system is located at the point on the spicule's longitudinal mid-plane directly above the left trench edge. We assume that the spicule deforms in the plane whose normal vector is $\hat{e}_1 \times \hat{e}_2$.

We adopted the principal strain failure hypothesis originally proposed by Saint-Venant (Gross and Seelig, 2011). That is, we assume that each spicule fails when the maximum principal strain within it reaches a critical value, ϵ_f , which we call its bending failure strain. The infinitesimal strain tensor is $\epsilon = \epsilon_{ij}\hat{e}_i \otimes \hat{e}_j$, where “ \otimes ” denotes the dyadic product and repeated indices imply summation over the integers 1, 2, 3 (Einstein summation convention). We assume that the spicules' deformations satisfy the kinematic hypothesis of elastica theory (Dym and Shames, 1973; Hjelmstad, 2007). That is, we assume that cross-sections in the undeformed configuration (see Fig. 4 (A)) remain planar in the deformed configuration (see Fig. 4 (B)), and that there exists a neutral plane in the structure.¹ Based on micrographs of the spicules' undeformed configurations (see Fig. 3 (A), (C)), we assume that in the undeformed configuration, the spicule's neutral plane has zero curvature. As a result of this kinematic hypothesis, the only nonzero strain component is $\epsilon_{11} = r\kappa(z)$, where $r \in [0, r_0(z)]$ is a material point's distance from the neutral plane in the undeformed configuration, $r_0(z)$ is the spicule's cross-sectional radius, and $\kappa(z)$ is the curvature of the spicule's neutral plane (Dym and Shames, 1973; Hjelmstad, 2007). Since ϵ_{11} is the only nonzero strain component, it is also the maximum principal strain. This means that

$$\epsilon_f = r_0(z^*)\kappa(z^*), \quad (4)$$

where $z^* = \text{argmax}\{r_0(z)\kappa(z) : z \in [0, L]\}$, and $\kappa(z)$ belongs to the spicule's deformed configuration just before it fails.

We assign $r_0(z^*)$ to be the radius of the cross-section at which the spicule fails. We measured $r_0(z^*)$ by collecting and imaging the broken spicule fragments after each bending test (see Section 2.4). A histogram of $r_0(z^*)$ for the *E.a.* and *T.a.* spicules is shown in Fig. 5 (A). The mean \pm standard deviation of $r_0(z^*)$ are 19.7 ± 2.8 μm and 17.2 ± 2.0 μm for the *E.a.* and *T.a.* spicules, respectively.

We computed $\kappa(z^*)$ using the following procedure. It has been shown that both *E.a.* and *T.a.* spicules are axisymmetric (Monn et al., 2015; Monn and Kesari,). As a consequence of this symmetry, a spicule's neutral plane is the same as its longitudinal mid-plane in its undeformed configuration (see Fig. 4 (A)). We built a discrete representation of the neutral plane using a set of points $(z_i, w_i)_{i=1,\dots,n}$, which we manually selected from the micrograph of the spicule's deformed configuration just before failure (see Fig. 4 (C), (D)). The abscissae, z_i , were spaced in the \hat{e}_1 direction in increments of roughly

¹ The neutral plane is a surface composed of material points whose shape changes as the structure deforms. In the undeformed configuration the neutral plane is normal to the \hat{e}_2 direction. Material fibers of infinitesimal length belonging to the neutral plane and oriented in the \hat{e}_1 direction in the undeformed configuration do not change length as the structure deforms.

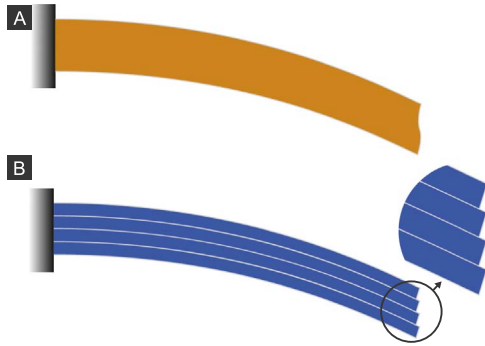


Fig. 6. (A), (B) The deformed configurations of a monolithic and a multi-layered beam, respectively. Adjacent layers in the multi-layered beam are able to slide past one another as the beam is bent.

15–20 μm . As a result, the total number of points in the discrete representation, n , varied from 57 to 137. For each z_i , we manually chose w_i so that the point (z_i, w_i) coincided with the spicule's neutral plane. We built a continuous representation of the neutral plane by fitting a fourth order polynomial, $f(z) = \sum_{j=0}^4 a_j z^j$, to the (z_i, w_i) data, and computed the curvature of the spicule's neutral plane as $\kappa(z) = f''(z)/(1 + f'(z)^2)^{3/2}$ (see Fig. 4 (D), (E) and Fig. 5 (B)). To obtain $\kappa(z^*)$ we assumed that both the strain, $r_0(z)\kappa(z)$, and the curvature, $\kappa(z)$, attain their maximum values at the same z position. Hence, we approximate $\kappa(z^*) = \max\{\kappa(z) : z \in [0, L]\}$.

Finally, we used Eq. (4) to compute each spicule's bending failure strain (see Fig. 5 (C)). The mean \pm standard deviation of ϵ_f for the *E.a.* and *T.a.* spicules are 0.0377 ± 0.0043 and 0.0158 ± 0.0042 , respectively.

4. Conclusion

We showed that the bending failure strain of the *E.a.* spicules is \approx 140% larger than that of the *T.a.* spicules. We do not believe that this result is a consequence of the *E.a.* spicules' silica being intrinsically stronger than the *T.a.* spicules' silica. Rather, we believe that the *E.a.* spicule's architecture allows it to deform differently than a monolithic beam, and reduces the maximum strain that the spicule experiences for a given $\kappa(z)$ compared to a monolithic beam. In Section 3 we compute the *E.a.* spicules' bending failure strains by approximating their kinematics using elastica theory (i.e., we assume that the strain is given by $\epsilon_{11} = r\kappa(z)$). However, a more refined mechanics model that accounts for the spicule's architecture is needed to understand the mechanism(s) underlying the enhancement of *E.a.* spicules' bending failure strains. Specifically, while ϵ_{11} increases linearly with the distance, r , from the neutral plane in a monolithic beam, this may not be true for the spicules.

As a preliminary hypothesis we consider a beam model in which adjacent concentric layers slide relative to one another. Consider, for example, the 2D layered beam shown in Fig. 6 (B). Since adjacent layers are not glued together, when the beam is bent they are able to slide relative to one another like stacked sheets of paper. This allows the layered beam to undergo larger deformations than a monolithic beam with the same cross-section (see Fig. 6 (A)) before the strain in any layer meets the failure criterion. Consequently, the layered beam would appear to have a larger bending failure strain since it would have a larger curvature before it failed. While the mechanics of this 2D analog and the concentrically layered *E.a.* spicules are different, a similar mechanism could be operating in the *E.a.* spicules. That is, like in the 2D analog, the sliding of adjacent layers may allow strain to be redistributed across the spicule's cross-section.

Euler-Bernoulli beam theory, which assumes that both the strain and displacements are small, does not predict that the strain would redistribute even when adjacent layers can slide relative to one another.

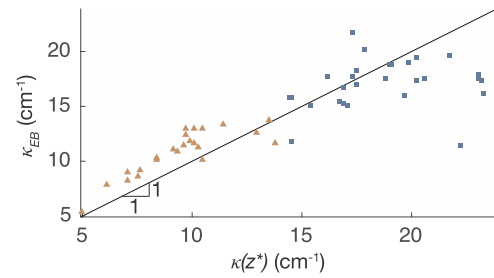


Fig. 7. Comparison of the measured spicule failure curvatures with Euler-Bernoulli beam theory predictions. The failure curvature predicted by Euler-Bernoulli beam theory, κ_{EB} , is compared to the curvatures measured from optical micrographs using the elastica theory (see Section 3 for details). The curvatures, $\kappa(z^*)$ and κ_{EB} , of the *E.a.* and *T.a.* spicules are shown as blue squares and orange triangles, respectively. (For interpretation of the references to color in this figure legend, the reader is referred to the web version of this article.)

However, as can be seen in our experiments (see Fig. 3 (D)), the *E.a.* spicules undergo very large displacements before they fail. If we compute the curvature of the *E.a.* spicules using Euler-Bernoulli beam theory, we find that the theory underpredicts the spicules' maximum curvature. Specifically, the maximum curvature of the *E.a.* spicules predicted by Euler-Bernoulli beam theory is

$$\kappa_{EB} = \frac{12F_f}{k_s L^2}, \quad (5)$$

where F_f is the applied force at failure, L is the trench's span, and k_s is the slope of the linear portion of the spicule's F - w_0 data (see Section 2.2) (Gere and Timoshenko, 1997).

We compare κ_{EB} to the maximum curvature measured directly from the images of the spicules' deformed configurations (see Section 3) for both the *E.a.* and *T.a.* spicules in Fig. 7. From this comparison we see that for small $\kappa(z^*)$, the Euler-Bernoulli theory provides a reasonable approximation for the actual curvature of the spicule. However, for most *E.a.* spicules $\kappa(z^*)$ is large and the difference between the Euler-Bernoulli theory prediction and the measured curvature increases. Specifically, Euler-Bernoulli theory underpredicts the maximum curvature of the *E.a.* spicules. Therefore, a new mechanics model of the *E.a.* spicule that not only accounts for the *E.a.* spicules' architecture but also considers large displacements is needed to further investigate the proposed strain redistribution hypothesis.

Acknowledgements

We thank James Weaver for providing us with the *T.a.* spicules and introducing us to this fascinating structural biological material. We thank Jarod Ferreira for his help constructing and calibrating the mechanical testing device. This work was supported by National Science Foundation [Mechanics of Materials and Structures Program, grant number 1562656]; and the American Society of Mechanical Engineers [Haythornthwaite Young Investigator Award].

References

- Aizenberg, J., Sundar, V.C., Yablon, A.D., Weaver, J.C., Chen, G., 2004. Biological glass fibers: correlation between optical and structural properties. *Proc. Natl. Acad. Sci. USA* 101 (10), 3358–3363.
- Aizenberg, J., Weaver, J.C., Thanawala, M.S., Sundar, V.C., Morse, D.E., Fratzl, P., 2005. Skeleton of *Euplectella* sp.: structural hierarchy from the nanoscale to the macroscale. *Science* 309 (5732), 275–278.
- Barber, A.H., Lu, D., Pugno, N., 2015. Extreme strength observed in limpet teeth. *J. R. Soc. Interface* 12 (105), 20141326.
- Barthelat, F., 2014. Designing nacre-like materials for simultaneous stiffness, strength and toughness. *Optimum materials, composition, microstructure and size. J. Mech. Phys. Solids* 73, 22–37.
- Bernstein, B.T., 1962. Elastic properties of polycrystalline tungsten at elevated temperatures. *J. Appl. Phys.* 33 (6) [2140–2140].
- Cappella, B., Dieter, G., 1999. Force-distance curves by atomic force microscopy. *Surf. Sci. Rep.* 34, 1–104.

- Chen, P.Y., Lin, A.Y.M., Lin, Y.S., Seki, Y., Stokes, A.G., Peyras, J., Olevsky, E.A., Meyers, M.A., McKittrick, J., 2008. Structure and mechanical properties of selected biological materials. *J. Mech. Behav. Biomed. Mater.* 1 (3), 208–226.
- Chen, X., Beyerlein, I.J., Brinson, L.C., 2009. Curved-fiber pull-out model for nanocomposites. part 1. Bonded stage formulation. *Mech. Mater.* 41 (3), 279–292.
- Dym, C.L., Shames, I.H., 1973. *Solid mechanics*, Springer. Ch. The Elastica, pp. 516–521.
- Espinosa, H.D., Rim, J.E., Barthelat, F., Buehler, M.J., 2009. Merger of structure and material in nacre and bone-perspectives on de novo biomimetic materials. *Progress. Mater. Sci.* 54 (8), 1059–1100.
- Gere, J.M., Timoshenko, S.P., 1997. *Mechanics of materials*, PWS. Ch. Deflections of beams, pp. 351–384.
- Gross, D., Seelig, T., 2011. *Fracture mechanics: with an introduction to micromechanics*, Springer Science & Business Media. Ch. Classical Fracture and Failure Hypotheses, pp. 39–48.
- Hjelmstad, K.D., 2007. *Fundamentals of structural mechanics*, Springer Science & Business Media. Ch. Derivation of the Nonlinear Planar Beam Theory, pp. 390–397.
- Jackson, A.P., Vincent, J.F.V., Turner, R.M., 1988. The mechanical design of nacre. *Proc. R. Soc. Lond. B: Biol. Sci.* 234 (1277), 415–440.
- Leys, S., 2003. Comparative study of spiculogenesis in demosponge and hexactinellid larvae. *Microsc. Res. Tech.* 62 (4), 300–311.
- Müller, W.E., Wang, X., Cui, F.-Z., Jochum, K.P., Tremel, W., Bill, J., Schröder, H.C., Natalio, F., Schloßmacher, U., Wiens, M., 2009. Sponge spicules as blueprints for the biofabrication of inorganic-organic composites and biomaterials. *Appl. Microbiol. Biotechnol.* 83 (3), 397–413.
- Meyers, M.A., McKittrick, J., Chen, P.Y., 2013. Structural biological materials: critical mechanics-materials connections. *Science* 339 (6121), 773–779.
- Monn, M.A., Kesari, H. A new structure-property connection in the skeletal elements of the marine sponge *tethya aurantia* that guards against buckling instability. *Scientific Reports*.
- Monn, M.A., Weaver, J.C., Zhang, T., Aizenberg, J., Kesari, H., 2015. New functional insights into the internal architecture of the laminated anchor spicules of *euplectella aspergillum*. *Proc. Natl. Acad. Sci. USA* 112 (16), 4976–4981.
- Oliver, W.C., Pharr, G.M., 1992. An improved technique for determining hardness and elastic modulus using load and displacement sensing indentation experiments. *J. Mater. Res.* 7 (06), 1564–1583.
- Rabiei, R., Bekah, S., Barthelat, F., 2010. Failure mode transition in nacre and bone-like materials. *Acta Biomater.* 6 (10), 4081–4089.
- Rim, J.E., Zavattieri, P., Juster, A., Espinosa, H.D., 2011. Dimensional analysis and parametric studies for designing artificial nacre. *J. Mech. Behav. Biomed. Mater.* 4 (2), 190–211.
- Sarà, M., Manara, E., 1991. Cortical structure and adaptation in the genus *tethya* (porifera, demospongiae). In: *Fossil and Recent Sponges*. Springer, pp. 306–312.
- Simmons, G., Wang, H. Single crystal elastic constants and calculated aggregate properties.
- Van Soest, R.W., Boury-Esnault, N., Vacelet, J., Dohrmann, M., Erpenbeck, D., De Voogd, N.J., Santodomingo, N., Vanhoorne, B., Kelly, M., Hooper, J.N.A. Global diversity of sponges (porifera). *PLoS One*. 7(4).
- Wang, L., Cui, Y., Qin, Q., Wang, H., Wang, J., 2016. Helical fiber pull-out in biological materials. *Acta Mech. Solida Sin.* 29 (3), 245–256.
- Weaver, J.C., Aizenberg, J., Fantner, G.E., Kisailus, D., Woesz, A., Allen, P., Fields, K., Porter, M.J., Zok, F.W., Hansma, P.K., Fratzl, P., Morse, D.E., 2007. Hierarchical assembly of the siliceous skeletal lattice of the hexactinellid sponge *euplectella aspergillum*. *J. Struct. Biol.* 158 (1), 93–106.
- Weaver, J.C., Milliron, G.W., Allen, P., Miserez, A., Rawal, A., Garay, J., Thurner, P.J., Seto, J., Mayzel, B., Friesen, L.J., Chmelka, B.F., Fratzl, P., Aizenberg, J., Dauphin, Y., Kisailus, D., Morse, D.E., 2010. Unifying design strategies in demosponge and hexactinellid skeletal systems. *J. Adhes.* 86 (1), 72–95.
- Weaver, J.C., Milliron, G.W., Miserez, A., Evans-Lutterodt, K., Herrera, S., Gallana, I., Mershon, W.J., Swanson, B., Zavattieri, P., DiMasi, E., Kisailus, D., 2012. The stomatopod dactyl club. A formidable damage-tolerant biological hammer. *Science* 336 (6086), 1275–1280.
- Wegst, U.G.K., Bai, H., Saiz, E., Tomsia, A.P., Ritchie, R.O., 2015. Bioinspired structural materials. *Nat. Mater.* 14 (1), 23–36.
- Yang, R., Zaheri, A., Gao, W., Hayashi, C., Espinosa, H.D. Afm identification of beetle exocuticle: Bouligand structure and nanofiber anisotropic elastic properties. *Advanced Functional Materials* 27 (6).